NEMA NU-4 2008 performance evaluation of Xtrim-PET: A prototype SiPM-based preclinical scanner

Mahsa Amirrashedi, and Saeed Sarkar
Department of Medical Physics and Biomedical Engineering, Tehran University of Medical Sciences, Tehran, Iran
Research Center for Molecular and Cellular Imaging, Tehran University of Medical Sciences, Tehran, Iran

Pardis Ghafarian
Chronic Respiratory Diseases Research Center, National Research Institute of Tuberculosis and Lung Diseases (NRITLD), Shahid Beheshti University of Medical Sciences, Tehran, Iran
PET/CT and Cyclotron Center, Masih Daneshvari Hospital, Shahid Beheshti University of Medical Sciences, Tehran, Iran

Reza Hashemi Shahraki
Department of Medical Physics and Biomedical Engineering, Tehran University of Medical Sciences, Tehran, Iran
Research Center for Molecular and Cellular Imaging, Tehran University of Medical Sciences, Tehran, Iran

Parham Geramifar
Research Center for Nuclear Medicine, Shariati Hospital, Tehran University of Medical Sciences, Tehran, Iran

Habib Zaidi[a)]
Division of Nuclear Medicine and Molecular Imaging, Geneva University Hospital, Geneva CH-1211, Switzerland
Geneva University Neurocenter, Geneva University, CH-1205, Geneva, Switzerland
Department of Nuclear Medicine and Molecular Imaging, University of Groningen, University Medical Center Groningen, 9700 RB, Groningen, Netherlands
Department of Nuclear Medicine, University of Southern Denmark, 500 Odense, Denmark

Mohammad Reza Ay[a)]
Department of Medical Physics and Biomedical Engineering, Tehran University of Medical Sciences, Tehran, Iran
Research Center for Molecular and Cellular Imaging, Tehran University of Medical Sciences, Tehran, Iran

(Received 22 April 2019; revised 5 August 2019; accepted for publication 6 August 2019; published 24 September 2019)

Purpose: Xtrim-PET is a newly designed Silicon Photomultipliers (SiPMs)-based prototype PET scanner dedicated for small laboratory animal imaging. We present the performance evaluation of the Xtrim-PET scanner following NEMA NU-4 2008 standards to help optimizing scanning protocols which can be achieved through standard and reliable system performance characterization.
Methods: The performance assessment was conducted according to the National Electrical Manufacturers Association (NEMA) NU-4 2008 standards in terms of spatial resolution, sensitivity, counting rate performance, scatter fraction and image quality. The *in vivo* imaging capability of the scanner is also showcased through scanning a normal mouse injected with ^{18}F-FDG. Furthermore, the performance characteristics of the developed scanner are compared with commercially available systems and current prototypes.
Results: The volumetric spatial resolution at 5 mm radial offset from the central axis of the scanner is 6.81 μl, whereas a peak absolute sensitivity of 2.99% was achieved using a 250–650 keV energy window and a 10 ns timing window. The peak noise-equivalent count rate (NECR) using a mouse-like phantom is 113.18 kcps at 0.34 KBq/cc with 12.5% scatter fraction, whereas the NECR peaked at 82.76 kcps for an activity concentration level of 0.048 KBq/cc with a scatter fraction of 25.8% for rat-like phantom. An excellent uniformity (3.8%) was obtained using NEMA image quality phantom. Recovery coefficients of 90%, 86%, 68%, 40% and 12% were calculated for rod diameters of 5, 4, 3, 2 and 1 mm, respectively. Spill-over ratios for air-filled and water-filled chambers were 35% and 25% without applying any correction for attenuation and Compton scattering effects.
Conclusion: Our findings revealed that beyond compactness, lightweight, easy installation and good energy resolution, the Xtrim-PET prototype presents a reasonable performance making it suitable for preclinical molecular imaging-based research. [https://doi.org/10.1002/mp.13785]

Key words: detectors, NEMA standard, performance evaluation, PET, small animal imaging

1. INTRODUCTION

Recent years have witnessed widespread interest and increased popularity in translational molecular imaging-based biomedical research stimulated largely by the availability of dedicated small-animal scanners. Among the promising animal imaging modalities, positron emission tomography (PET), as a highly versatile research tool, has further enabled the quantitative assessment of disease progression and metabolic evaluation of cellular biology.[1] Clinical whole-body PET scanners are not suitable as they were not optimized for preclinical imaging in terms of sensitivity and spatial resolution.[2] As a consequence of the growing attractiveness of these miniaturized scanners for the preclinical research portfolio, various designs of dedicated small animal PET prototypes were introduced over the past two decades, with many of them being commercially available.[3–15] To ensure a fair comparison between different scanners and objectively optimize data acquisition and reconstruction protocols for a variety of applications, the National Electrical Manufacturers Association (NEMA) provided a specific standard (NEMA NU-4) for the evaluation and performance characterization of preclinical PET scanners in terms of spatial resolution, sensitivity, scatter fraction, count rate characteristics and overall imaging performance.[16] Subsequently, the majority of commercial small-animal PET scanners and prototype models have been characterized according to the NEMA NU-4 standards.[3–14,17–,29]

PET scanners featuring SiPM-based detectors exhibit a multitude of advantages over photomultiplier tubes (PMTs)-based designs. This includes lower operation voltage, higher quantum efficiency, miniature size, robustness and immunity to magnetic field, which facilitates integration with other imaging modalities, such as magnetic resonance imaging (MRI).[30,31] The compact, portable and cost-effective SiPM-based preclinical scanner evaluated in this work (Xtrim-PET) was recently developed by our group.[32] The high modularity and scalability of Xtrim-PET design confers a much more customizable and highly flexible scheme, shortens the redesign cycle, simplifies and speeds up system services, development and upgrade procedures driven by user requirements and technological advancement (e.g. increasing the number of axial detector rings to achieve higher sensitivity and/or provide dynamic whole body imaging capability, extending the transaxial field-of-view (FOV) by increasing the number of detector blocks for other potential applications, for example, non-human primates, or integration with other imaging modalities). Besides, thermal stability of the detectors is achieved through active cooling of the detector arrays by mini add-on fans on SiPM heat-sinks, which reduces design complexity and provides substantial cost savings. Above all, a simple temperature monitoring circuit is incorporated in the system to control and keep the operating temperature of the detector head at 25 ± 1°C. This cooling approach enables the scanner to operate satisfactorily in room temperature.

Herein, we presented the first performance evaluation of Xtrim-PET scanner using NEMA-NU 2008 standards. The overall imaging capability of the Xtrim-PET is also assessed through scanning a normal mouse injected with ^{18}F-FDG. In addition, the performance characteristics of the scanner are compared with commercially available systems as well existing prototypes dedicated for small-animal imaging.

2. MATERIALS AND METHODS

2.A. System description

Xtrim-PET is a newly designed preclinical prototype scanner dedicated for imaging small laboratory animals, including mice and rats (Fig. 1). A detailed description of the Xtrim-PET system and readout electronics has been reported elsewhere.[32–34] The overall design parameters of the system are summarized in Table I. In brief, the system is composed of 10 detector blocks arranged around a decagon like geometry having 166 mm inner diameter, leading to a maximum transaxial and axial fields-of-view of 100 and 50.3 mm, respectively. Each block consists of 24 (tangential) × 24 (axial) Cerium-doped Lutetium Yttrium Orthosilicate (LYSO: Ce) scintillator arrays measuring 2 × 2 × 10 mm^3 with a pixel pitch of 2.1 mm and read out by 12 × 12 arrays of Silicon Photomultiplier (SiPM) pixels (SensL, Ireland).[35] Overall, there are 24 detector rings (one block ring) and 5760 LYSO scintillation crystals within the gantry.

Each detector head houses LYSO scintillators, SiPM arrays, and multiplexing boards. Detector heads are enclosed in an aluminum box and are connected to the digital front-end (DFE) board through a flexible flat cable (FFC). All the information regarding photons interaction (such as timing, positioning and energy) are determined in DFE board. For this purpose, a modified scrambled cross-wire (SCR) channel reduction method was implemented. The 144 SiPM pixels are reduced into 3 × 3(9) virtual sections with 4 × 4(16) pixels in each section. In the modified SCR approach, instead of summed cathode signals, the fast analog output of nine sections were used to detect the triggered section and to extract timing information. The interaction position inside the fired section as well as photons energy were determined by the 16 pixel signals. Each pixel signal is the summation of the signals arising from the pixels with identical location in different sections. After amplification, these analogue signals are digitized through 8 channels analog to digital converters (ADCs) with a sample rate of 50-MHz and then are fed into the Field Programmable Gate Array (FPGA). A more detailed description can be found in REFS.[32–34]

Leading Edge Discrimination (LED) algorithm was considered to measure time pick off of the event. Moreover, Time to digital converters (TDCs) were used to determine the exact arrival time of annihilation photons. The system is also equipped with an easily attached/detached animal bed. The bed includes a dedicated heating pad and can be translated axially and transaxially using a motorized stage to enable multi-bed acquisition.

Xtrim-PET acquires three-dimensional (3D) data in the coincidence list mode format (LMF), providing spatial coordinates, energy and timing information of incident photons

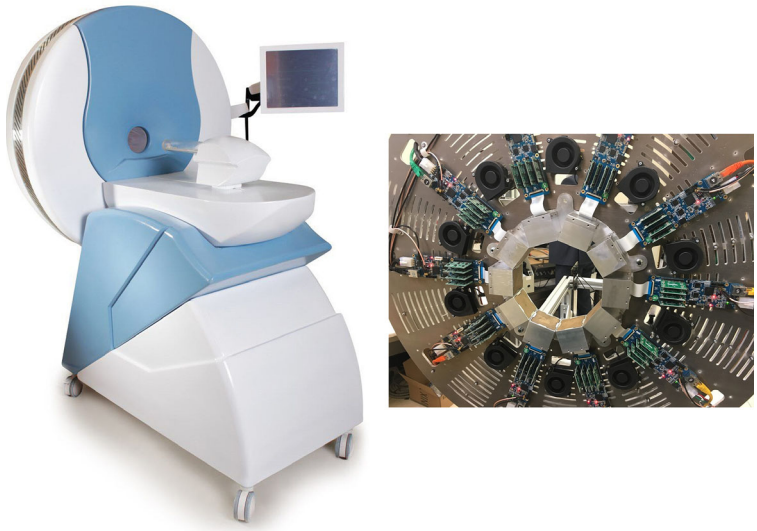

FIG. 1. Photograph of the Silicon Photomultipliers (SiPM)-based XTRIM-PET scanner dedicated for imaging small laboratory animals (left) and arrangement of detector blocks arranged in a ring with 166 mm diameter (right). [Color figure can be viewed at wileyonlinelibrary.com]

TABLE I. Physical characteristics and design parameters of the Xtrim-PET scanner.

Detectors	
Scintillator type	LYSO
Number of blocks	10
Number of detector rings	24
Crystal dimensions	$2 \times 2 \times 10$ mm^3
Crystal pitch	2.1×2.1 mm^2
Number of crystals per detector ring	240
Total number of crystals	5760
Detector ring diameter	166 mm
SiPM array	12×12
SiPM pixel size	3×3 mm^2
SiPM pixel pitch	4.2×4.2 mm^2
System	
Maximum width of energy window	100–800 keV
Maximum transaxial field-of-view	100 mm
Axial field-of-view	50.3 mm
Bore opening	120 mm
Coincidence timing window	10 ns
Acquisition mode	List mode format

within each detector block. The information packet for each event is then transferred from the detector block to a Digital Coincidence Processing Unit (DCPU). Prompt and random coincidences are separated in the DCPU board before reaching the acquisition computer for further processing and calibration steps. After applying positioning and energy corrections using pre-calculated look up tables (LUTs), true events are histogrammed into 3D sinograms and normalized through component-based normalization [36]. To generate two-dimensional (2D) sinograms ($256 \times 256 \times 47$) prior to reconstruction, single-slice rebinning (SSRB)[37] and Fourier rebinning (FORE)[38] algorithms are implemented on the software available to end-users. An in-house reconstruction package is provided which includes filtered backprojection (FBP) and ordered subsets expectation maximization (OSEM) algorithms for reconstructing 2D sonograms.[39] Images are usually reconstructed with a $128 \times 128 \times 47$ or a $256 \times 256 \times 47$ matrix size. Owing to the short axial field-of-view, whole body images are acquired with 2 bed positions for mouse and 3 bed positions for rat studies. Data correction for quantitative imaging including attenuation and scattering are under development and are not available on the current version of the software.

2.B. Spatial resolution

The spatial resolution of the Xtrim-PET scanner was measured using a point source containing 19 MBq of ^{18}F aqueous solution (we used ^{18}F instead of ^{22}Na due to easier accessibility). The point source was centred both axially and transaxially and scanned for 1 min with an energy window of 250–650 keV and coincidence timing window of 10 ns. The same experiment was repeated for 5, 10, 15, 25 mm radial offsets at the centre of the field-of-view (CFOV) and one fourth of the axial field-of-view (AFOV). For each acquisition, at least 10^5 counts were collected and histogrammed to 3D sinograms. The 3D sinograms were rebinned using SSRB algorithm with a ring difference of ten. Subsequently, 2D sinograms were reconstructed with FBP using a 0.39×0.39 mm^2 voxel grid and 1.05 mm slice thickness in accordance with the NEMA NU-4 2008 standards. For all slices, one-dimensional (1D) profiles through the pixel with maximum count density were generated tangentially, radially and axially. The spatial resolution was determined as the full width at half maximum (FWHM) and full width at tenth maximum (FWTM) by interpolation between adjacent pixels at half and one tenth of the

peak values, respectively. The volumetric spatial resolution is reported as the product of the axial, tangential and radial resolutions. It should be noted that random coincidences, positron range effect, photon non-collinearity and source dimension were not corrected following NEMA guidelines.

2.C. Sensitivity

To assess system sensitivity, ^{18}F point source with an activity of 11.1 kBq was used. The point source was centred on the bed and moved with 2 mm axial increments along the axial axis to cover the whole AFOV. More than 10^5 counts were collected for 70 s at each source position with two different settings for the energy window (250–650 keV and 400–700 keV). Three-dimensional sinograms were rebinned with a ring difference of 24 using SSRB without applying further corrections. For each acquisition i, bins in a spatial window of 1 cm around the peak value of each sinogram row were selected and summed to estimate the number of total events. The summed sinogram is then divided by the acquisition time $T_{acq,i,}$ to calculate the source count rate R_i.

In addition, the background count rate of LYSO crystals, $R_{B,i}$ (cps) was determined using a 5 min blank scan. It should be noted that the same spatial mask was applied on background sinograms.

Finally, the sensitivity for acquisition i, S_i (cps/Bq), was calculated as:

$$S_i = \frac{(R_i - R_{B,i})}{A}, \tag{1}$$

where A is the average source activity during acquisition. The absolute sensitivity (%) was determined according to Eq. 2 by correcting S_i for the branching ratio of the source:

$$S_{A,i} = \frac{S_i}{0.967} \times 100 \tag{2}$$

For both energy windows, the absolute sensitivity was plotted against axial planes as reported in the NEMA NU-4 standards. In addition, the sensitivity of the scanner for an energy window of 250–650 keV was computed by imaging a 555 kBq ^{18}F line source during 5 min followed by conversion of the sensitivity of the point source at the CFOV as described elsewhere.[24,40] The percentage difference of the absolute peak sensitivity between the two methods is given by the following:

$$\Delta(\%) = \frac{(S_{point} - S_{line})}{S_{point}} \times 100 \tag{3}$$

2.D. Count loss and scatter fraction

Mouse-like and rat-like phantoms were fabricated as described in the NEMA NU-4 standards. For this purpose, a 3.2 cm hole was drilled at 1 cm away from the centre of the mouse phantom, which is made of a solid polyethylene cylinder with a diameter of 25 mm and a length of 70 mm. Another 150 mm long cylinder with 50 mm diameter was constructed to mimic a rat phantom with a 3.2 mm cylinder hole at 17.5 mm from the centre to accommodate the line source.

The count rate performance of the scanner was measured using the mouse-like and rat-like phantoms on two separate occasions with initial activities of 37 and 61.05 MBq, respectively. The phantoms were positioned at the CFOV and along the z-axis of the scanner. For the mouse phantom, 12 acquisitions with 30 min duration were recorded until the randoms to true ratio reaches approximately below 1%. For rat phantom, acquisitions were performed with 15 min intervals. In all experiments, the energy and timing windows were set to 250–650 keV and 10 ns, respectively, which are the recommended settings for operation of the scanner. The last data acquisition sequence for each phantom (where the randoms rate is <1% of the trues rate) was used for calculating the scatter fraction (SF).

Two-dimensional sinograms were generated using SSRB to calculate the SF. For each projection in each slice, the pixel with maximum value was found and shifted to the central bin of the sinogram. By aligning all peaks for each sinogram raw, all projections were summed and a 1D profile of the summed projections plotted. In compliance with NEMA standards, all the pixels beyond 8 mm of phantom edges were set to zero. To calculate the combined effects of scatter, random and intrinsic counts rates (R_{s+r+I}), all pixels located beyond 7 mm of the central pixel were considered to be scatter and random events. Linear interpolation was performed between two pixels at 7 mm distance from the central pixel to obtain the remaining part of $R_{s+r+I,}$ which was located under the peak area. Finally, true and scatter count rates were determined according to Eqs (4) and (5).

$$R_{true} = R_{total} - R_{s+r+Int} \tag{4}$$

$$R_{scatter} = R_{total} - R_{true} - R_{random} - R_{Int} \tag{5}$$

R_{total} is the total counts in the sinogram. The intrinsic count rate (R_{Int}) due to natural radioactivity present in LYSO crystals was estimated by scanning each phantom (without any activity) for 30 min. R_{random} was assessed from the randoms sinogram (negligible for SF calculation). Finally, the scatter fraction for each plane was calculated as:

$$Scatter\,fraction(SF) = \frac{R_{scatter}}{R_{scatter} + R_{true}} \tag{6}$$

For each set of acquisition, the noise equivalent count rate (NECR) was obtained using Eq. (7) and plotted versus the average activity concentration.

$$NECR = \frac{R_{true}^2}{R_{total}} \tag{7}$$

2.E. Image quality characteristics

As detailed by the NEMA NU-4 standards, the image quality (IQ) phantom is a cylinder made up of polymethylmethacrylate with 30 mm diameter and 50 mm length. The

phantom consists of three distinct sections to measure image quality metrics: a uniform region for uniformity assessment, 5 fillable rods with diameters ranging between 1 and 5 mm to quantify recovery coefficients (RCs) for each rod size and two cold chambers filled with water and air to determine the spill-over ratios (SORs).

The NEMA IQ phantom was fabricated and filled with ^{18}F-FDG aqueous solution (3.7 MBq) and scanned for 20 min. Normalization and randoms correction were performed prior to reconstruction. Three-dimensional sinograms were rebinned using FORE and reconstructed using 2D OSEM with 5 iterations and 5 subsets in $0.39 \times 0.39 \times 1.05$ mm^3 voxel size. A volume of interest (VOI) with 22.5 mm diameter (covering 75% of the inner diameter of the phantom) and 10 mm length was placed in the uniform section of the IQ phantom. The mean, maximum, minimum and percentage standard deviation (STD%) of the counts were reported.

To assess RC values and related STDs as specified in the NEMA NU-4 standard, all the slices encompassing the central 10 mm of the hot spheres were averaged to generate a single transverse slice. Over each rod size on the averaged image, a region of interest (ROI) with a diameter twice the diameter of the hot rod was drawn and the location of the pixel with maximum value to generate the line profile along the axial direction of each road. The mean value of the line profile for each rod size to the mean value of the uniform section was reported as RC. The respective STD for each rod is then given by the following:

$$STD_{RC(\%)} = 100 \times \sqrt{\left(\frac{STD_{lineprofile}}{Mean_{lineprofile}}\right)^2 + \left(\frac{STD_{uniform}}{Mean_{uniform}}\right)^2} \quad (8)$$

For calculating SORs, two VOIs with 4 mm diameter and 7.5 mm length were defined inside the cold chambers. The ratio of the mean in each cold region to the mean value of the uniform section was reported as SOR. The STD for each chamber was computed using Eq. (8).

2.F. Small-animal study

Prior to undertaking this study, institutional approval was obtained from the ethics committee of Tehran University of Medical Sciences (Approval ID: IR.TUMS.MEDICINE.REC.1397.004). A 20 g healthy mouse (female, 12 weeks) was intravenously injected with an activity of 8.2 MBq of ^{18}F-FDG and anesthetized with intraperitoneal administration of 0.2 ml ketamine/xylazine based on the ethics code in our department. PET acquisition started 1-h post-injection and lasted for 15 min using an energy window of 250–650 keV (3 beds, 5 min per bed position). During the scanning period, the animal was kept warm (37^{0}C) on a dedicated heating pad installed on the animal bed. After correcting the data for detector efficiency and random events, 3D sinograms were rebinned using FORE and reconstructed using 2D OSEM (5 iterations, 5 subsets) with a voxel size of $0.78 \times 0.78 \times 1.05$ mm^3.

3. RESULTS

Figures 2 and 3 illustrate the results of the spatial resolution in terms of FWHM and FWTM at two different axial positions. The radial FWHM at 5 mm radial offset from the CFOV is 2.01 mm and reaches 2.56 at 25 mm radial offset while at the same distances, the tangential resolution ranges between 1.95 and 2.23 mm. The axial spatial resolution shows higher dependence on the radial offset and degrades from 1.74 to 3.25 mm for the same transverse locations. The volumetric resolution at 5 mm radial offset of the central slice of the AFOV and ¼ of AFOV is 6.81 and 11.57 μl, respectively.

The count rate performances for the mouse-like and rat-like phantoms versus the average activity concentration (MBq/cc) are plotted in Figs. 4 and 5, respectively. The peak NECR for the mouse-like phantom is 113.18 kcps at 0.34 MBq/cc whereas the peak true events rate is 126.1 kcps at 0.46 MBq/cc. For the rat-like phantom, the NECR reaches its maximum value of 82.76 kcps at 48 kBq/cc with a maximum true count rate of 94.44 kcps at 52.8 kBq/cc.

SF values were determined as 12.5% and 25.8% for mouse and rat phantoms, respectively. Axial sensitivity profiles for two window settings were plotted as a function axial offset and presented in Fig. 6. The peak absolute sensitivity and average absolute sensitivity with an energy window of 400–700 keV and timing window of 10 ns are 2.2% and 1.18%, respectively. Since, the axial extension of Xtrim-PET is shorter than the length of mouse and rat phantoms, the total absolute sensitivity for mouse and rat length are equal to the total system sensitivity which is about 30.39%. Furthermore, using a 250–650 keV energy window leads to a peak absolute sensitivity of 2.99% at CFOV and average sensitivity of 1.72%. The peak absolute sensitivity measured, using a ^{18}F line source was 2.86% for energy window of 250–650 keV with relative difference of $\Delta = 4.35\%$ in comparison to the stepping point source measurements.

Transverse views from the different sections of the IQ phantom are illustrated in Fig. 7. The results of the uniformity metrics obtained from the IQ phantom are reported in

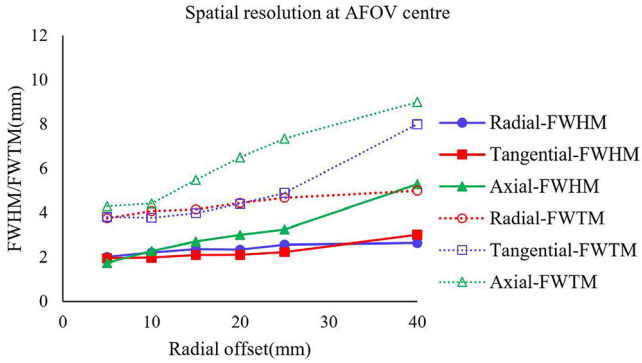

FIG. 2. Spatial resolution in the terms of full width at half maximum (solid lines) and full width at tenth maximum (dashed lines) as a function of radial offset at the centre of the axial field-of-view. [Color figure can be viewed at wileyonlinelibrary.com]

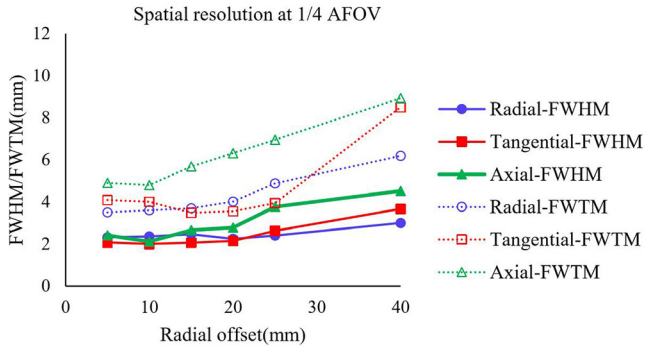

FIG. 3. Spatial resolution in the terms of full width at half maximum (solid lines) and full width at tenth maximum (dashed lines) as a function of radial offset at ¼ axial field-of-view. [Color figure can be viewed at wileyonlinelibrary.com]

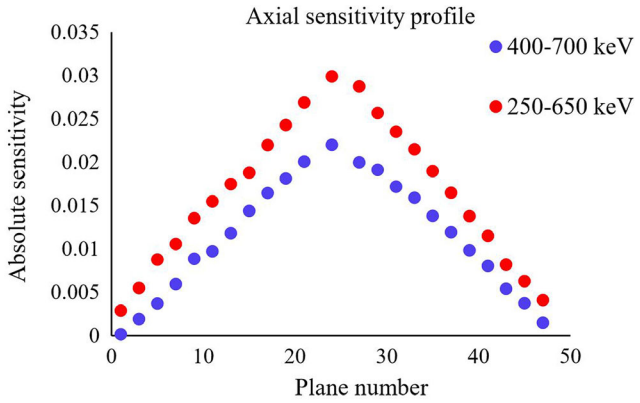

FIG. 4. Axial sensitivity profile against the axial plane number for two energy windows [250–650 keV] and [400–700 keV]. [Color figure can be viewed at wileyonlinelibrary.com]

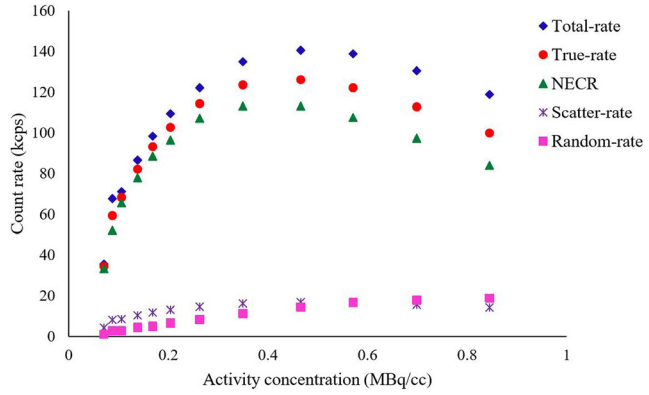

FIG. 5. Count rate performance for the mouse-like National Electrical Manufacturers Association phantom as a function of average activity concentration. [Color figure can be viewed at wileyonlinelibrary.com]

Table II. RC values and respective STDs (error bars) are depicted as a function of rod diameter in Fig. 8. In addition, SOR values of air-filled and water-filled chambers highlighting the contribution of attenuation and scatter events are 0.35 ± 0.1 and 0.25 ± 0.2, respectively.

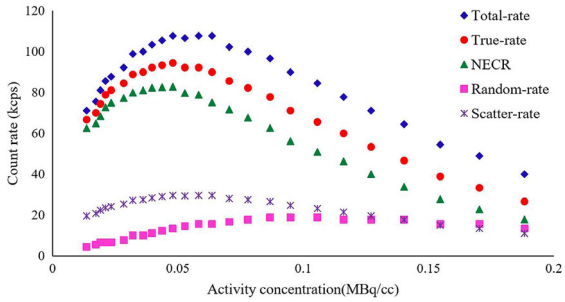

FIG. 6. Count rate performance for the rat-like National Electrical Manufacturers Association phantom as a function of average activity concentration. [Color figure can be viewed at wileyonlinelibrary.com]

Figure 9 depicts whole-body PET images of a healthy mouse obtained by scanning three bed positions. The images clearly show high ^{18}F-FDG accumulation in the Harderian glands, heart region and spinal cord.

4. DISCUSSION

The overall performance of the Xtrim-PET prototype model was evaluated following the NEMA NU—4 2008 standard, specifically addressing the performance characterization of preclinical PET scanners in terms of spatial resolution, sensitivity, count rate and overall image quality. The most significant factor affecting the intrinsic spatial resolution of PET scanners is the detector size, 2 mm for the Xtrim-PET. Previous studies showed that that the spatial resolution of the majority of PET scanners is slightly larger than crystal dimensions.[12] The radial FWHM of our scanner is 2.01 at 5 mm radial offset obtained from ^{18}F source, which is close to or better than the corresponding values reported for FLEX Triumph X-PET (2.0 mm),[7] microPET R4 (2.13 mm),[12] microPET P4 (2.29 mm),[12] Mosaic HP (2.32 mm),[12] ClairvivoPET (2.16 mm),[6] and Trans-PET/CT X5 (2.11)[27] with approximately similar crystal dimensions. The effective transaxial resolution of our prototype is 2.02 at 5 mm radial distance whereas the ratio of the effective transverse resolution to the crystal size is about 1.02, which is in line with those reported for the microPET P4 (1.02), microPET Focus 120 (1.18), microPET Focus 220 (1.19), Inveon (1.08), Mosaic HP (1.17), Argus (1.14) and VrPET (1.15).[12] A number of currently available preclinical PET scanners have shown superior spatial resolution compared to the Xtrim-PET owing to the smaller crystal cross-section, which results in higher cost and also manufacturing complexity.[12,20,25] Another cost-effective approach to improve the spatial resolution consists in utilizing monolithic scintillators as adopted in the β-cube design.[3] Besides the good spatial resolution, this system presents excellent spatial resolution uniformity across the transaxial FOV owing to DOI capabilities of monolithic crystals.

Moreover, it is worth emphasizing that we used an ^{18}F point source with 1.1 mm diameter as an alternative to 0.25–0.3 mm ^{22}Na to measure the spatial resolution, which would

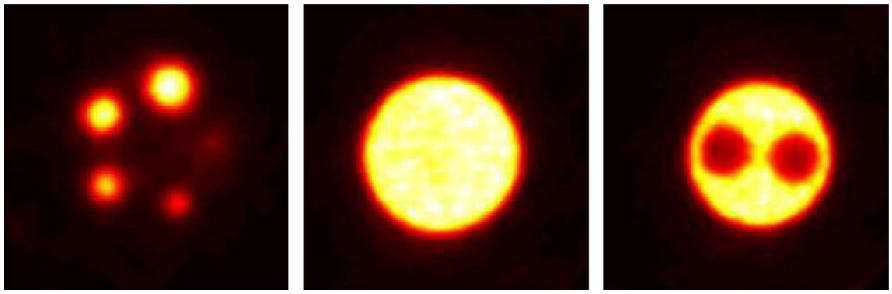

FIG. 7. Transverse views of the hot rods (left), uniform section (middle) and cold chambers (right) of the image quality phantom. [Color figure can be viewed at wileyonlinelibrary.com]

TABLE II. Results of uniformity and spill over ratios for cold chambers evaluated using the IQ phantom.

Uniform region				Water chamber		Air chamber	
Mean	STD	Maximum	Minimum	SOR	STD	SOR	STD
0.0067	3.82%	0.0079	0.0055	25%	2%	35%	1%

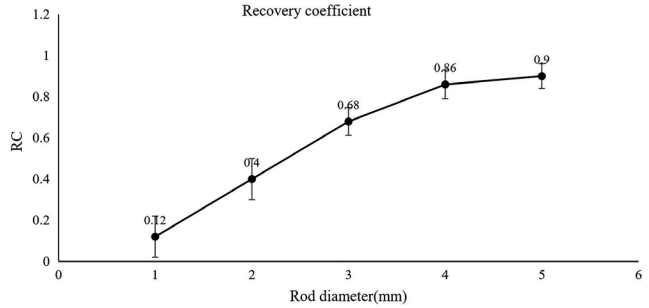

FIG. 8. Recovery coefficients and respective standard deviations (error bars) for each rod diameter of the IQ phantom. The images were reconstructed using FORE + OSEM2D with 5 iterations and 4 subsets.

adversely affect the measurements owing to inhomogeneity and larger dimensions of the ^{18}F point source. The average radial, tangential and axial FWHMs within 25 mm radial distance from the centre of the scanner are 2.29, 2.07 and 2.59, respectively. These reduced to 2.01, 1.75 and 2.32 mm, respectively, after deconvolution for the effect of source size.

The simulation study performed by Sanaat et al.[41] reported the spatial resolution and sensitivity of the Xtrim-PET scanner for pixelated and monolithic crystal configurations. The spatial resolution values reported in this study are slightly lower than those reported by Sanaat et al. The discrepancies between two studies could be attributed to differences in source diameters, energy windows, reconstruction algorithms and image matrix sizes. In addition, the sensitivity reported by Sanaat et al. with an energy window of 400–650 keV (1.8%) is lower than the one obtained in the present study (2.2%) for an energy window of 400–700 keV.

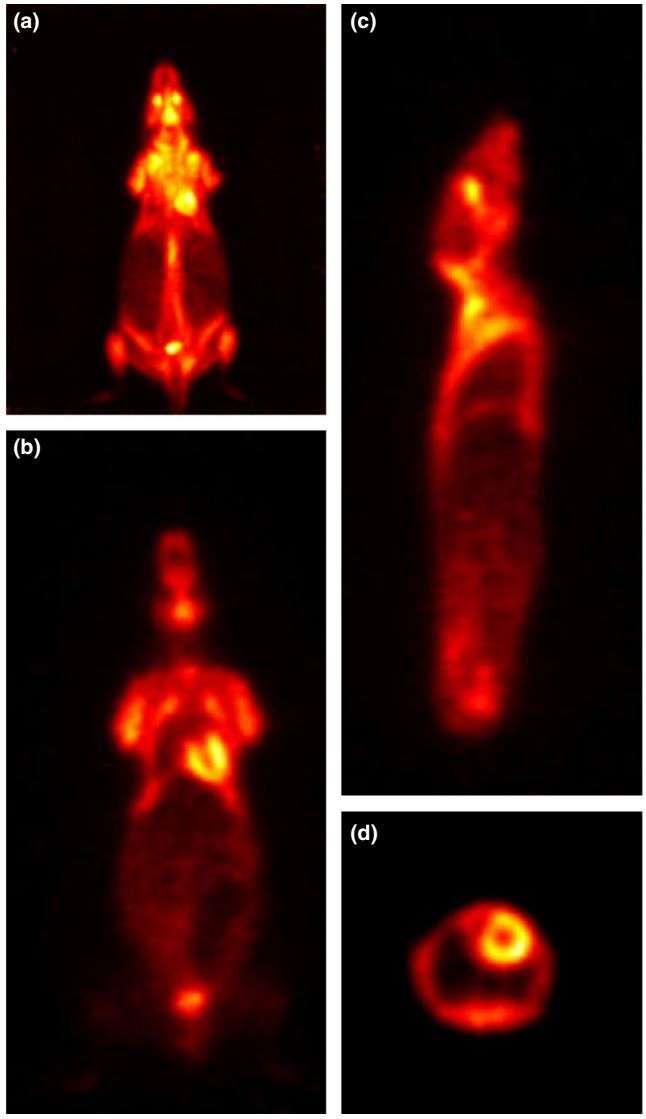

FIG. 9. Maximum intensity projection (a), sagittal (b), coronal (c) and transverse views (d) of a normal mouse injected with an activity of 8.2 MBq of ^{18}F-FDG scanned 1-h post-injection for 15 min. [Color figure can be viewed at wileyonlinelibrary.com]

The slight non-uniformity of the spatial resolution across the transaxial FOV, particularly in the axial direction (Figures 2 and 3), is severely hampered by SSRB and FBP

reconstruction for scanners with polygon or other irregular geometries.[6,20,25,27] This issue is more severe for small-animal imaging which could be explained by the combined effects of rebinning, lack of scatter and attenuation corrections and multi-bed reconstruction where the reconstructed images of each bed position are stitched together considering the axial overlap. However, the axial spatial resolution and uniformity of reconstructed images could be resolved through accurate system modelling and 3D iterative reconstruction which is being implemented on the system.

The count rate study in terms of random, true, scatter, total and NECR for mouse and rat phantoms demonstrate the system good detection capability in lower activity concentration used for routine applications. Expectedly higher scatter fraction was obtained for rat-like phantom in comparison to mouse-like phantom which is owing to increasing the numbers of scattered event with object size. Scatter fraction for mouse-like phantom (12%) compares favorably well with scanners using the same energy window like ClairvivoPET (17.7%),[6] MRS-PET (21%),[17] NanoPET/CT (15%),[28] NanoScan PET/MRI (17.3%),[21] and RAYCAN(14%).[27]

One of the most interesting features of the present scanner is the SiPM-based detection scheme, which results in relatively good energy and timing resolution. Through employing time walk correction, a coincidence timing resolution of 1.85 ns FWHM and 4.4 ns FWTM was achieved between two identical blocks,[33] which enables to reduce the number of detected random events, even when imaging high activities. Furthermore, the energy resolution as well as the peak to valley ratio for different bias voltages were measured by irradiating detector arrays with Ge-68 rod sources located at 10 cm distance. The overall energy resolution of the system was about 12.4% with a mean peak to valley ratio of 43.8 at 25°C temperature and 28 V bias voltage, which is better than the Inveon (14.6%),[22] NanoPET(19%),[28] LabPET (25%)[10] and Argus (26%).[5] Moreover, it is slightly better than recently designed LYSO/SiPM-based systems, such as MRS-PET (14.6%),[17] MADPET4 (13.7%),[20] RAYCAN (15%),[27] Hyperion (12.7%)[42] and scanners reported by Lee et al. (13.2%),[23] Ko et al. (14.2%)[43] and Goertzen et al. (12.5%)[44] but lower than the β-cube PET scanner (12%).[3]

The axial sensitivity profile represents the typical triangular shape which falls linearly from the centre to periphery of both sides of the AFOV. The peak absolute sensitivity of the Xtrim-PET is 2.2% for an energy window of 400–700 keV and increases up to 2.99% by increasing the width of the energy window (250–650 keV). The achieved sensitivity of the Xtrim-PET is close to the ones achieved by scanners with longer AFOV, such as ClearPET (3.03%),[12] rPET-1(1%),[45] LabPET4&8 (1.4, 2.6%),[12] Mosaic HP (2.83%),[12] microPET models (1.9, 2.06%), VrPET (2.22%), Trans-PET (2.04%),[29] microFocus220 (2.28%),[12] RAYCAN (1.7%),[27] Hyperion (2.6%),[25] and the system reported by Lee et al. (1.5%).[23] Moreover, compared to recently designed high-resolution PET inserts, the sensitivity profile is more homogenous owing to gapless axial configuration of the Xtrim-PET.[3,20,25,27] The recommended energy and timing windows for data acquisition are 400–650/700 keV and 6 ns, respectively. However, a 250–650 keV energy window and 10 ns coincidence window (widest windows) were used in this preliminary work at the expense of a higher scatter and random fractions owing to the short axial FOV of the scanner which degrades the sensitivity.

In spite of the fact that there are many factors influencing the counting rate performance of the scanners but generally higher sensitivity leads to higher NECR values at lower activity concentrations. The peak NECR for Xtrim-PET (113.8 kcps, peak absolute sensitivity of 2.99%) is comparable to respective values for systems with approximately similar peak detection sensitivity including ClearPET (72 kcps, 3.03%),[12] Argus (117 kcps, 4.32%),[12] VrPET (74 kcps, 2.36%),[12] and exceeds the reported values for current generation of PET inserts such as MADPET4 (29 kcps, 0.76%),[20] PET insert by Ko et al. (42.2 kcps, 3.36%),[43] PET insert by Stortz et al. (20.8 kcps, 2.2%),[18] Lee et al. (21.1 kcps,1.5%),[23] Albira (16.5 kcps, 2.5%)[11] and MRS-PET (61.9 kcps, 4.7%).[17]

Despite the absence of quantitative corrections for attenuation and scattering, the results achieved for the IQ phantom (3.84% uniformity) outperformed some of the commercial scanners and currently manufactured prototype models applying quantitative corrections, except the NanoScan PET/MRI (3.5%)[21] and Hyperion II^D (3.7%).[25] This is in part due to the normalization method applied, which compensates the transaxial gaps during the normalization procedure. The RC values achieved by the Xtrim-PET scanner agree well with values reported for other preclinical systems.[9,12,18,27] As expected, the spill-over ratios are worse compared to other preclinical scanners, which can be attributed to not performing scatter correction and using a wider energy window (250–650 keV) in the current study owing to the low sensitivity of the scanner. The main concern in the Xtrim-PET design is the small axial FOV which reduces the detection efficiency and degrades the axial uniformity, particularly in multi-bed reconstruction schemes. Extending the axial coverage of the Xtrim-PET scanner is straightforward owing to the modularity of the design and low cost readout electronics. Overall, the quantitative analysis of the IQ phantom indicates that additional corrections, including attenuation, Compton scatter and parallax error need to be considered to improve image quality and quantitative accuracy of the Xtrim-PET prototype.

5. CONCLUSION

The NEMA NU-4 2008 standard was followed to evaluate the performance characteristics of the Xtrim-PET prototype model. A comparison with previously developed preclinical PET scanners was also presented. The results demonstrated that the system has good spatial resolution and sensitivity, which makes it suitable for small animal studies. The main conceptual design guiding the fabrication of this scanner is producing a compact and modular configuration with acceptable performance in terms of spatial resolution, sensitivity,

count-rate capability, energy and temporal resolution without sacrificing the other features, particularly fabrication and maintenance complexity and cost. It is obvious that using a smaller crystal size and increasing the number of detector rings will improve the scanner's spatial resolution and sensitivity, respectively. Our motivation was to design a cost-effective configuration using relatively large crystals and short axial FOV while keeping the overall scanner performance acceptable. Moreover, it is worth to note that the modularity and upgradability of the scanner makes it possible to easily add new features to improve scanner performance. Further improvements in system sensitivity and axial uniformity could be achieved through extending the axial FOV of the prototype to further facilitate whole-body dynamic imaging capabilities. In addition, the quantitative capability of the current version of the system is being improved through the implementation of dedicated data correction techniques, including attenuation and scattering as well as statistical image reconstruction with accurate system modelling to further enhance overall image quality. Overall, our assessment proves the practical and technical suitability of the Xtrim-PET for use in the preclinical imaging domain using molecular imaging probes.

ACKNOWLEDGMENTS

This work was supported through grant No. 36847 from the Tehran University of Medical Sciences and the Swiss National Science Foundation under grant SNFN 320030_176052.

[a)]Authors to whom correspondence should be addressed. Electronic mails: habib.zaidi@hcuge.ch, mohammadreza_ay@sina.tums.ac.ir; Telephones: +41 22 372 7258, +9821 64053255; Fax: +41 22 372 7169.

REFERENCES

1. Levin CS, Zaidi H. Current trends in preclinical PET system design. *PET Clin*. 2007;2:125–160.
2. Stout DB, Zaidi H. Preclinical multimodality imaging in vivo. *PET Clin*. 2008;3:251–273.
3. Krishnamoorthy S, Blankemeyer E, Mollet P, Surti S, Van Holen R, Karp JS. Performance evaluation of the MOLECUBES β-CUBE-a high spatial resolution and high sensitivity small animal PET scanner utilizing monolithic LYSO scintillation detectors. *Phys Med Biol*. 2018;63:155013.
4. Belcari N, Camarlinghi N, Ferretti S, et al. NEMA NU-4 performance evaluation of the IRIS PET/CT preclinical scanner. *IEEE Trans Rad Plasma Med Sci*. 2017;1:301–309.
5. Wang Y, Seidel J, Tsui BM, Vaquero JJ, Pomper MG. Performance evaluation of the GE healthcare eXplore VISTA dual-ring small-animal PET scanner. *J Nucl Med*. 2006;47:1891–1900.
6. Sato K, Shidahara M, Watabe H, et al. Performance evaluation of the small-animal PET scanner ClairvivoPET using NEMA NU 4–2008 standards. *Phys Med Biol*. 2015;61:696–711.
7. Prasad R, Ratib O, Zaidi H. Performance evaluation of the FLEX Triumph™ X-PET scanner using the NEMA NU-04 standards. *J Nucl Med*. 2010;51:1608–1615.
8. Prasad R, Ratib O, Zaidi H. NEMA NU-04-based performance characteristics of the LabPET-8™ small animal PET scanner. *Phys Med Biol*. 2011;56:6649–6664.
9. Canadas M, Embid M, Lage E, Desco M, Vaquero JJ, Perez JM. NEMA NU 4–2008 performance measurements of two commercial small-animal PET scanners: ClearPET and rPET-1. *IEEE Trans Nucl Sci*. 2011;58:58–65.
10. Bergeron M, Cadorette J, Bureau-Oxton C, et al. Performance evaluation of the LabPET12, a large axial FOV APD-based digital PET scanner. IEEE Nuclear Science Symposium Conference Record (NSS/MIC); Oct. 24 -Nov. 1, 2009.
11. Balcerzyk M, Kontaxakis G, Delgado M, et al. Initial performance evaluation of a high resolution Albira small animal positron emission tomography scanner with monolithic crystals and depth-of-interaction encoding from a user's perspective. *Meas Sci Technol*. 2009;20:104011.
12. Goertzen AL, Bao Q, Bergeron M, et al. NEMA NU 4–2008 comparison of preclinical PET imaging systems. *J Nucl Med*. 2012;53:1300–1309.
13. Gu Z, Taschereau R, Vu NT, et al. Performance evaluation of G8, a high-sensitivity benchtop preclinical PET/CT tomograph. *J Nucl Med*. 2019;60:142–149.
14. Kemp BJ, Hruska CB, McFarland AR, Lenox MW, Lowe VJ. NEMA NU 2–2007 performance measurements of the Siemens Inveon preclinical small animal PET system. *Phys Med Biol*. 2009;54:2359–2376.
15. Wang L, Zhu J, Liang X, et al. Performance evaluation of the Trans-PET (R) BioCaliburn(R) LH system: a large FOV small-animal PET system. *Phys Med Biol*. 2015;60:137–150.
16. National Electrical Manufacturers Association. NEMA Standards Publication NU 4 – 2008. Performance Measurements of Small Animal Positron Emission Tomographs. Rosslyn, VA: National Electrical Manufacturers Association; 2008.
17. Vrigneaud JM, McGrath J, Courteau A, et al. Initial performance evaluation of a preclinical PET scanner available as a clip-on assembly in a sequential PET/MRI system. *Phys Med Biol*. 2018;63:125007.
18. Stortz G, Thiessen JD, Bishop D, et al. Performance of a PET insert for high resolution small animal PET/MR imaging at 7T. *J Nucl Med*. 2017;59:536–542.
19. Perez-Liva M, Viel T, Yoganathan T, et al. Performance evaluation of the PET component of a hybrid PET/CT-ultrafast ultrasound imaging instrument. *Phys Med Biol*. 2018;63:19NT01.
20. Omidvari N, Cabello J, Topping G, et al. PET performance evaluation of MADPET4: a small animal PET insert for a 7 T MRI scanner. *Phys Med Biol*. 2017;62:8671–8692.
21. Nagy K, Toth M, Major P, et al. Performance evaluation of the small-animal nanoScan PET/MRI system. *J Nucl Med*. 2013;54:1825–1832.
22. Magota K, Kubo N, Kuge Y, Nishijima K, Zhao S, Tamaki N. Performance characterization of the Inveon preclinical small-animal PET/SPECT/CT system for multimodality imaging. *Eur J Nucl Med Mol Imaging*. 2011;38:742–752.
23. Lee S, Choi Y, Jung JH, et al. Performance evaluation of a small animal PET scanner a high level of multiplexing and charge-signal transmission. *Phys Med Biol*. 2019;64:045015.
24. Knoess C, Siegel S, Smith A, et al. Performance evaluation of the microPET R4 PET scanner for rodents. *Eur J Nucl Med Mol Imaging*. 2003;30:737–747.
25. Hallen P, Schug D, Weissler B, et al. PET performance evaluation of the small-animal Hyperion II(D) PET/MRI insert based on the NEMA NU-4 standard. *Biomed Phys Eng Express*. 2018;4:065027.
26. Gu Z, Taschereau R, Vu NT, et al. NEMA NU-4 performance evaluation of PETbox4, a high sensitivity dedicated PET preclinical tomograph. *Phys Med Biol*. 2013;58:3791–3814.
27. Teuho J, Han C, Riehakainen L, et al. NEMA NU 4–2008 and in vivo imaging performance of RAYCAN trans-PET/CT X5 small animal imaging system. *Phys Med Biol*. 2019;64:115014.
28. Szanda I, Mackewn J, Patay G, et al. National Electrical Manufacturers Association NU-4 performance evaluation of the PET component of the NanoPET/CT preclinical PET/CT scanner. *J Nucl Med*. 2011;52:1741–1747.
29. Zhu J, Wang L, Kao C-M, Kim H, Xie Q. Performance evaluation of the Trans-PET®BioCaliburn® SH system. *Nucl Instrum Methods Phys Res A*. 2015;777:148–153.
30. Zaidi H, Becker M. The Promise of hybrid PET/MRI: technical advances and clinical applications. *IEEE Sign Proc Mag*. 2016;33:67–85.

31. Cal-Gonzalez J, Rausch I, Shiyam Sundar LK, et al. Hybrid imaging: instrumentation and data processing. *Front Phys*. 2018;6:47.
32. Zeraatkar N, Sajedi S, Kaviani S, et al. Development of a preclinical PET system based on pixelated LYSO crystals and SiPM arrays. IEEE Nuclear Science Symposium and Medical Imaging Conference (NSS/MIC); 21–28 Oct. 2017.
33. Sajedi S, Zeraatkar N, Taheri M, et al. Generic high resolution PET detector block using 12 × 12 SiPM array. *Biomed Phys Eng Express*. 2018;4:035014.
34. Sajedi S, Zeraatkar N, Taheri M, et al. A Generic, Scalable, and Cost-Effective Detector Front-End Block for PET. IEEE Nuclear Science Symposium and Medical Imaging Conference (NSS/MIC); 2017.
35. SensL D. C-Series Low Noise, Fast, Blue-Sensitive Silicon Photomultipliers Datasheet; 2014. http://sensl.com/downloads/ds/DS-MicroCseries.pdf
36. Badawi RD, Lodge MA, Marsden PK. Algorithms for calculating detector efficiency normalization coefficients for true coincidences in 3D PET. *Phys Med Biol*. 1998;43:189–205.
37. Daube-Witherspoon ME, Muehllehner G. Treatment of axial data in three-dimensional PET. *J Nucl Med*. 1987;28:1717–1724.
38. Defrise M, Kinahan PE, Townsend DW, Michel C, Sibomana M, Newport DF. Exact and approximate rebinning algorithms for 3-D PET data. *IEEE Trans Med Imaging*. 1997;16:145–158.
39. Yao R, Seidel J, Johnson CA, Daube-Witherspoon ME, Green MV, Carson RE. Performance characteristics of the 3-D OSEM algorithm in the reconstruction of small animal PET images. Ordered-subsets expectation-maximixation. *IEEE Trans Med Imaging*. 2000;19:798–804.
40. Elhami E, Boulding J, Goertzen AL. Variations on the NEMA NU4-2008 testing procedures and effect on the performance measurement results. IEEE Nuclear Science Symposium Conference Record; 23-29 Oct. 2011.
41. Sanaat A, Zafarghandi MS, Ay MR. Design and performance evaluation of high resolution small animal PET scanner based on monolithic crystal: a simulation study. *J Instrum*. 2019;14:P01005.
42. Schug D, Lerche C, Weissler B, et al. Initial PET performance evaluation of a preclinical insert for PET/MRI with digital SiPM technology. *Phys Med Biol*. 2016;61:2851–2878.
43. Ko GB, Yoon HS, Kim KY, et al. Simultaneous multiparametric PET/MRI with silicon photomultiplier PET and ultra-high-field MRI for small-animal imaging. *J Nucl Med*. 2016;57:1309–1315.
44. Goertzen AL, Stortz G, Thiessen JD, et al. First results from a high-resolution small animal SiPM PET insert for PET/MR imaging at 7T. *IEEE Trans Nucl Sci*. 2016;63:2424–2433.
45. Canadas M, Embid M, Lage E, Desco M, Vaquero JJ, Pérez JM. NEMA NU 4–2008 performance measurements of two commercial small-animal PET scanners: ClearPET and rPET-1. *IEEE Trans Nucl Sci*. 2011;58:58–65.